Nontrivial topology in the layered Dirac nodal-line semimetal candidate SrZnSb$_2$ with distorted Sb square nets

Jinyu Liu,[1,*] Pengfei Liu,[2] Kyle Gordon,[3] Eve Emmanouilidou,[1] Jie Xing,[1] David Graf,[4] Bryan C. Chakoumakos,[5] Yan Wu,[5] Huibo Cao,[5] Dan Dessau,[3] Qihang Liu,[2,6] and Ni Ni[1,†]

[1]*Department of Physics and Astronomy, University of California, Los Angeles, California 90095, USA*
[2]*Shenzhen Institute for Quantum Science and Technology and Department of Physics, Southern University of Science and Technology, Shenzhen, 518055, China*
[3]*Department of Physics, University of Colorado, Boulder, Colorado 80309, USA*
[4]*National High Magnetic Field Laboratory, 1800 E. Paul Dirac Drive, Tallahassee, Florida 32310, USA*
[5]*Quantum Condensed Matter Division, Oak Ridge National Laboratory, Oak Ridge, Tennessee 37831, USA*
[6]*Center for Quantum Computing, Peng Cheng Laboratory, Shenzhen, 518055, China*

Dirac states hosted by Sb/Bi square nets are known to exist in the layered antiferromagnetic AMnX$_2$ (A = CaSr/Ba/Eu/Yb, X=Sb/Bi) material family with the space group to be $P4/nmm$ or $I4/mmm$. In this paper, we present a comprehensive study of quantum transport behaviors, angle-resolved photoemission spectroscopy (ARPES), and first-principles calculations on SrZnSb$_2$, a nonmagnetic analog to AMnX$_2$, which crystalizes in the *pnma* space group with distorted square nets. From the quantum oscillation measurements up to 35 T, three major frequencies including $F_1 = 103$ T, $F_2 = 127$ T, and $F_3 = 160$ T are identified. The effective masses of the quasiparticles associated with these frequencies are extracted, namely, $m_1^* = 0.1$ m$_e$, $m_2^* = 0.1$ m$_e$, and $m_3^* = 0.09$ m$_e$, where m$_e$ is the free electron mass. From the three band Lifshitz-Kosevich fit, the Berry phases accumulated along the cyclotron orbit of the quasiparticles are 0.06π, 1.2π, and 0.74π for F_1, F_2, and F_3, respectively. Combined with the ARPES data and the first-principles calculations, we reveal that F_2 and F_3 are associated with the two nontrivial Fermi pockets at the Brillouin zone edge while F_1 is associated with the trivial Fermi pocket at the zone center. In addition, the first-principles calculations further suggest the existence of a Dirac nodal line in the band structure of SrZnSb$_2$.

I. INTRODUCTION

Topological semimetals including Dirac semimetals, Weyl semimetals, and topological node-line semimetals, representing new quantum states of matter, have attracted enormous attention in condensed matter physics [1–22]. In these systems, the low energy excitation of quasiparticles are of relativistic nature, i.e., they obey Dirac or Weyl equations [23]. From the band structure point of view, there exist linear bands with nontrivial topology near the Fermi level in the bulk state of these materials. Materials with such nontrivial topological bands may be found if guided by certain chemistry principles [24,25].

Topological bands generated by square nets of main group elements have been reported in many layered materials such as AMnX$_2$ (A = Ca/Sr/Ba/Eu/Yb, X=Sb/Bi) [26–37] and the WHM-type (W=Zr/Hf/La, H=Si/Ge/Sn/Sb, M=S/Se/Te) materials [12,13,16,38,39]. The AMnX$_2$ materials feature a common layered structure with alternative stacking of MnX$_4$ tetrahedral layers and A-X-A spacing layers. In the MnX$_4$ layers, Mn atoms sit at the centers of edge-sharing

tetrahedrons and develop antiferromagnetic (AFM) order with a Néel temperature around room temperature [32,33,40]. In the A-X-A layers, the X square net planes sandwiched by A atoms can host anisotropic Dirac or Weyl cones. The electronic structure in these materials is of quasi-2D nature because of the layered structure character. In addition, the magnetism can have an effect on the transport of relativistic fermions. In EuMnBi$_2$, the Dirac fermions in 2D Bi layers are confined by antiferromagnetically ordered Eu and Mn moments and give rise to bulk quantum Hall effect [29]. In Sr$_{1-y}$Mn$_{1-z}$Sb$_2$ ($y, z < 0.1$), where the Sb square net layers are distorted into Sb zigzag chains, the AFM ordered Mn moments are canted with a net ferromagnetic (FM) component whose magnitude varies with sample, and such a FM component affects the transport properties significantly [33]. In YbMnBi$_2$, the similar canted AFM order of Mn moments has been suggested to break the time reversal symmetry and lead to the emergence of type-II Weyl states [28,41,42].

However, it is still unclear if the antiferromagnetism plays an indispensable role for the presence of the Dirac fermion transport in the AMnX$_2$ family [43–46]. The elucidation of the topology of their nonmagnetic analogs will shed light on it. So far, the square nets of main group elements hosting Dirac states, which are found in the materials with a space group of $I4/mmm$ or $P4/nmm$, are all undistorted except the Sb
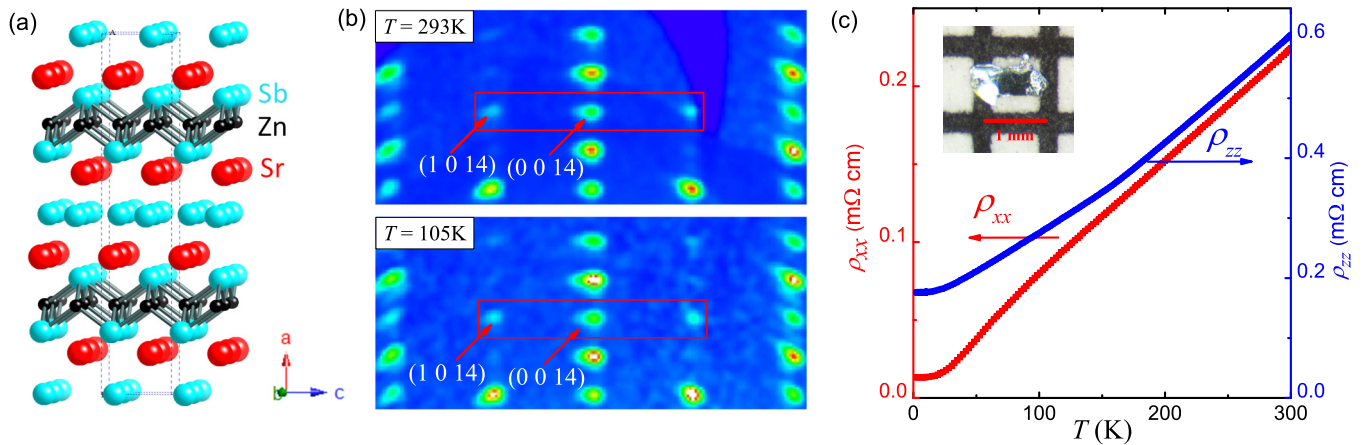
FIG. 1. (a) Crystal structure of SrZnSb$_2$. (b) Reciprocal lattice plane views at 293 K (top) and 105 K (bottom). (c) In-plane resistivity ρ_{xx} (red) and out-of-plane resistivity ρ_{zz} (blue) as a function of temperature from 2 K to 300 K. Inset is an optical image of a piece of SrZnSb$_2$ single crystal placed on a millimeter grid paper.

zigzag-chain layer in Sr$_{1-y}$Mn$_{1-z}$Sb$_2$. It has been pointed out by Bradlyn *et al.* in Ref. [24] that the topological behavior is insensitive to the in-plane distortion. More than 50 candidates composed by distorted square nets in space group *pnma*, including SrZnSb$_2$, are predicted to be topological nontrivial phases [24]. In this paper, we focus on SrZnSb$_2$, whose crystal structure is shown in Fig. 1(a). A previous study on SrZnSb$_2$ revealed linear magnetoresistance up to 9 T, suggesting the possible existence of Dirac fermion transport in the system [47]. We have grown SrZnSb$_2$ single crystals and confirmed its orthorhombic structure with a space group of *Pnma* at both 300 K and 105 K through single crystal x-ray diffraction [48]. We present the results from quantum transport measurements up to 35 T on SrZnSb$_2$ and reveal its detailed electronic structure with the input from first-principles calculations and ARPES experiments. From the quantum oscillations, we can derive three fundamental frequencies, i.e., $F_1 = 103$ T, $F_2 = 127$ T, and $F_3 = 160$ T and attribute them to a trivial quasi-2D Fermi pocket γ and two nontrivial quasi-2D Fermi pockets α and β, respectively. The Berry phases for the three frequencies agree well with the calculated values for α, β, and γ pockets. In addition, our first-principles calculations suggest this compound is a nodal-line Dirac semimetal candidate, which is of high interest for future study on this material.

II. EXPERIMENTAL METHODS

Single crystals of SrZnSb$_2$ were grown by the flux method. Sr and Zn chunks and Sb powder were mixed at a ratio of $1 : 1 : 5$ in an alumina crucible and sealed in a quartz tube under $1/3$ atmosphere of Ar gas. The tube was heated at $1050\,^\circ$C for 24 hours and slowly cooled to $650\,^\circ$C at a cooling rate of $3\,^\circ$C/hour. The excess Sb flux was then decanted by centrifuging. As shown in the inset of Fig. 1(c), shining platelike single crystals were obtained.

To determine whether the crystal remains in the *pnma* space group or undergoes some subtle structural distortion which has been observed in some of the 112 family of compounds, such as REAgSb$_2$ [49,50], single crystal diffraction measurement was performed. Single-crystal diffraction data

were collected at 300 K and 105 K using a Rigaku XtaLAB PRO diffractometer with graphite monochromated Mo $K\alpha$ radiation ($\lambda = 0.71073\,$Å) equipped with a Dectris Pilatus 200 K detector and an Oxford N-HeliX cryocooler. Numerous crystals were screened, and full data sets were collected for three pieces. Peak indexing and integration were done using the Rigaku Oxford Diffraction CrysAlisPro software [51]. An empirical absorption correction was applied using the SCALE3 ABSPACK algorithm as implemented CrysAlisPro. WinGX and SHELXL-2013 software packages were used for data processing and structure solution and refinement [52]. Crystal structure projections were made with VESTA [53].

The magnetotransport properties were measured in a Quantum Design physical property measurement system (QD PPMS) up to 9 T and at the National High Magnetic Field Lab (NHMFL) in Tallahassee, FL, up to 35 T. The ρ_{xx} was measured by a standard four probe method. To obtain ρ_{zz}, the current contacts were made into a ring shape at the top and bottom of the sample surfaces (*bc* plane) and the voltage contacts were placed at the center of the rings. The torque measurements were done using a piezoresistive cantilever connecting with a homemade Wheatstone bridge at NHMFL.

We applied density functional theory (DFT) by using the projector-augmented wave (PAW) pseudopotentials [55] with the exchange correlation of Perdew-Burke-Ernzerhof (PBE) form [56] as implemented in the Vienna *ab initio* simulation package (VASP) [57]. The energy cutoff was chosen 1.5 times as large as the values recommended in relevant pseudopotentials. The k-points-resolved value of Brillouin zone (BZ) sampling was $0.02 \times 2\pi/$Å. The total energy minimization was performed with a tolerance of 10^{-6} eV. The crystal structure was fully relaxed until the atomic force on each atom was less than 10^{-2} eV/Å. For the calculations with strain, atoms were relaxed with fixed lattice constants. Spin-orbit coupling (SOC) was included self-consistently throughout the calculations.

Angle-resolved photoemission spectroscopy (ARPES) measurements were conducted at the Advanced Light Source (ALS), BL4.0.3, with horizontally polarized, 98 eV light. The sample was held at 20 K during the measurements. We

TABLE I. Rietveld refinement results of $SrZnSb_2$ at 105 K and 293 K [54]. Crystal size is $150 \times 50 \times 10 \ \mu m^3$.

Formula	$SrZnSb_2$	$SrZnSb_2$
T (K)	105(1)	293(1)
Crystal system	orthorhombic	orthorhombic
Space group	*pnma*	*pnma*
a (Å)	22.835(9)	22.980(9)
b (Å)	4.3534(16)	4.3910(13)
c (Å)	4.4009(16)	4.4179(15)
V (Å)^3	437.5(3)	445.8(3)
θ	3.57–36.12	4.43–24.71
No. reflections collected	2879	4436
No. of variables	26	26
R_1	0.148	0.148
ωR_2	0.358	0.428
Goodness of fit	2.53	3.57
Largest diff. peak and hole (eÅ^{-3})	7.68, −6.54	9.80, −11.66

TABLE II. Atomic coordinates and equivalent isotropic displacement parameters of $SrZnSb_2$ at 105(1) K and 293(1) K.

105 K					
Atom	Site	x	y	z	U_{eq} (Å^2)
Sr	4c	0.1154(2)	1/4	0.721(1)	0.015(1)
Zn	4c	0.2502(8)	1/4	0.226(1)	0.019(2)
Sb1	4c	0.0004(4)	1/4	0.2213(9)	0.015(1)
Sb2	4c	0.3231(1)	1/4	0.7244(9)	0.011(1)
293 K					
Atom	Site	x	y	z	U_{eq}(Å^2)
Sr	4c	0.11514(2)	1/4	0.723(1)	0.023(2)
Zn	4c	0.250(1)	1/4	0.226(1)	0.030(3)
Sb1	4c	−0.0011(5)	1/4	0.222(1)	0.022(1)
Sb2	4c	0.3232(1)	1/4	0.720(1)	0.014(1)

estimated 44 meV energy resolution from the Fermi edge of the sample. The sample cleave appeared smooth under an optical microscope.

III. EXPERIMENTAL RESULTS

Like many other layered materials, the overall crystal quality of the samples was imperfect as evidenced by the lack of good agreement between symmetry equivalent reflections, and this disagreement could not be fully explained by twinning. Nevertheless, the best refinements (Table I) as well as reciprocal lattice plane views [Fig. 1(b)] are unable to discern any symmetry lowering between 105 K and 293 K. Neither additional reflections nor superlattice peaks were observed at 105 K. We also carefully checked the intensities of Bragg peaks at (0 0 14) and (1 0 14)/(0 1 14) at 105 K and 293 K collected on three crystals, which correspond to the ones at (0 0 7) and (1 0 7) in $LaAgSb_2$ [50], respectively. In $LaAgSb_2$, charge density wave was claimed by the observation of superlattice peaks at (1 0 7). This is not the case for $SrZnSb_2$ since the ratio of (1 0 14) or (0 1 14) to (0 0 14) shows no discernible changes at 105 K and 293 K. Therefore, our single crystal x-ray results do not suggest structural distortions in $SrZnSb_2$ (Table II).

The resistivity has been measured along the in-plane direction (ρ_{xx}) and out-of-plane direction (ρ_{zz}), as shown in Fig. 1(c). Both ρ_{xx} and ρ_{zz} show metallic behavior in the temperature range from 300 K to 2 K. The resistivity anisotropy ρ_{xx}/ρ_{zz} increases from ∼3 at the room temperature to 14 at 2 K, slightly higher than 12 for $CaMnBi_2$ [58], indicating the electronic structure is more anisotropic. Although a subtle slope change can be seen in ρ_{zz} around 150 K, as we have discussed, no clear evidence of possible structural distortion across this temperature is observed from our single crystal x-ray diffraction data. For ρ_{xx}, the residual resistivity ratio $[\rho_{xx}(300\,K)/\rho_{xx}(2\,K)]$ is ∼18, comparable to 15 for $SrMnBi_2$ [26], and much higher than 2 for $SrZnBi_2$ and 7 for $BaZnBi_2$ [44,46], which suggests good crystalline quality with reduced scattering from deficiencies of our samples.

We have performed magnetic torque measurements up to 35 T and probed strong dHvA oscillations in $SrZnSb_2$, as seen in Fig. 2(a). Figure 2(b) shows the dHvA oscillations after a polynomial background subtraction. The oscillations start from 5 T at $T = 2.1$ K and remain up to 50 K in high field range. As seen in Fig. 2(a), the oscillation peak at 30 T tends to broaden as the temperature goes down, implying that the Zeeman effect takes place in the high field range. To avoid any possible influence by Zeeman effect, we have performed the fast Fourier transform (FFT) in the field range between 5 T and 15 T as shown in Fig. 2(c), and resolved three frequencies with $F_1 = 103$ T, $F_2 = 127$ T, and $F_3 = 160$ T seen in the inset of Fig. 2(c). The effective masses of the quasiparticles corresponding to each of the oscillation frequencies can be obtained by fitting the temperature dependence of the FFT peak amplitude to the thermal damping term R_T in Lifshitz-Kosevich (LK) formula [59], i.e., $\frac{\Delta \rho}{\rho} \propto \alpha T \mu / [\bar{B} sinh(\alpha T \mu / \bar{B})]$, where $1/\bar{B}$ is the average inverse field when performing FFT analysis. As shown in Fig. 2(d), the fits result in three effective masses of 0.1 m_e, 0.1 m_e, and 0.09 m_e for F_1, F_2, and F_3, respectively. The quasiparticle effective masses in $SrZnSb_2$ are slightly lighter than those found in the Bi based 112 compounds like $BaZnBi_2$ [44–46] but heavier than those in other Sb based 112 compounds [32,33].

To map out the fermiology of $SrZnSb_2$, the evolution of the magnetic torque properties with field orientation has been investigated. As seen in Fig. 3(a), the dHvA oscillations show systematic shifts to higher fields as the field is tilted away from the a axis where the angle is defined as $\theta = 0°$. Figure 3(b) presents a color plot of the angular dependent FFT spectra, from which the revolution of FFT peaks can be clearly tracked. The obtained oscillating frequencies are plotted against the angle θ. F_1, F_2, and F_3 are well fitted by $F(\theta) = F_0/|\cos \theta|$, which suggests the corresponding Fermi surfaces corresponding to the quantum oscillations are quasi-2D like. Figure 3(c) shows the $MR(= [\rho_{xx}(B) - \rho_{xx}(0)]/\rho_{xx}(0))$ data measured at 2 K up to 9 T with different angles between the magnetic field and sample bc plane. The field is kept perpendicular to the in-plane current direction during rotation. When the field is applied perpendicularly to the sample bc plane, MR is ∼370% at 9 T. It gradually becomes smaller as the field is
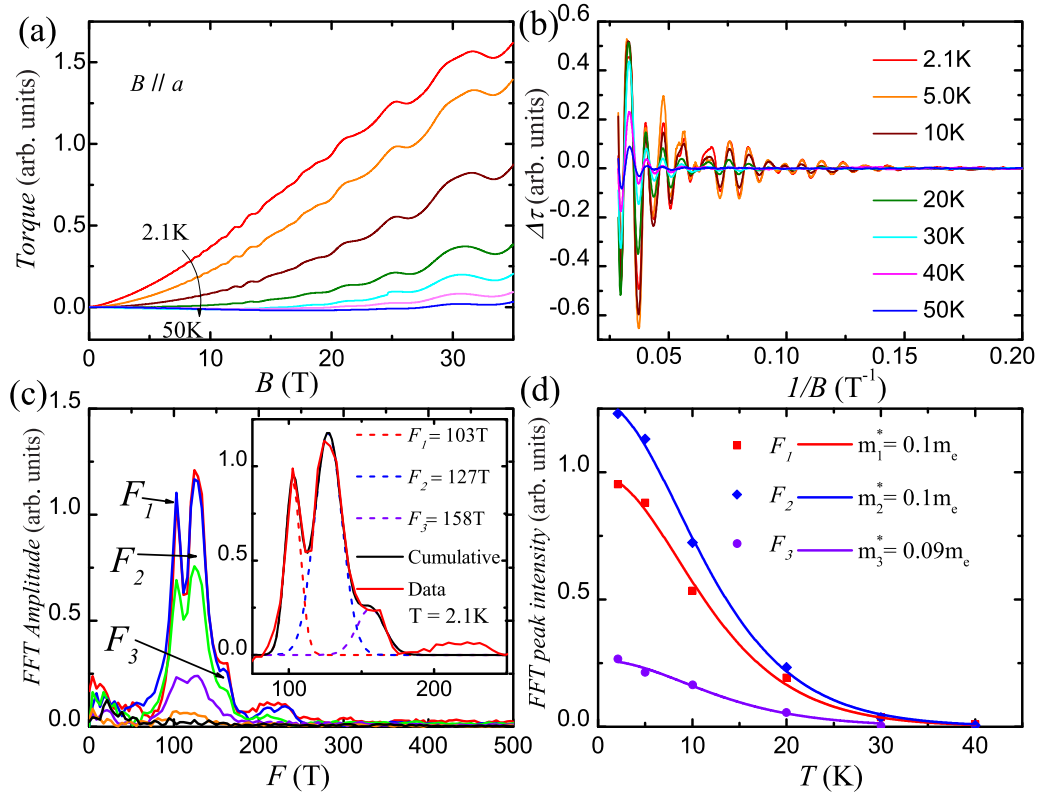
FIG. 2. (a) Field dependence of magnetic torque τ for SrZnSb$_2$ at different temperatures with magnetic field nearly parallel with out-of-plane direction. (b) The oscillatory part of the magnetic torque $\Delta\tau$. (c) The FFT spectra for $\Delta\tau$ between 5 T and 15 T at different temperatures. Three major oscillation frequencies are indicated. Inset: multipeak Gaussian fit of the FFT spectra to obtain the intensity of the three frequencies (only 2 K data is shown). (d) The temperature dependence of the FFT amplitude for the three frequencies and the fits to the thermal damping term of LK formula (solid lines).
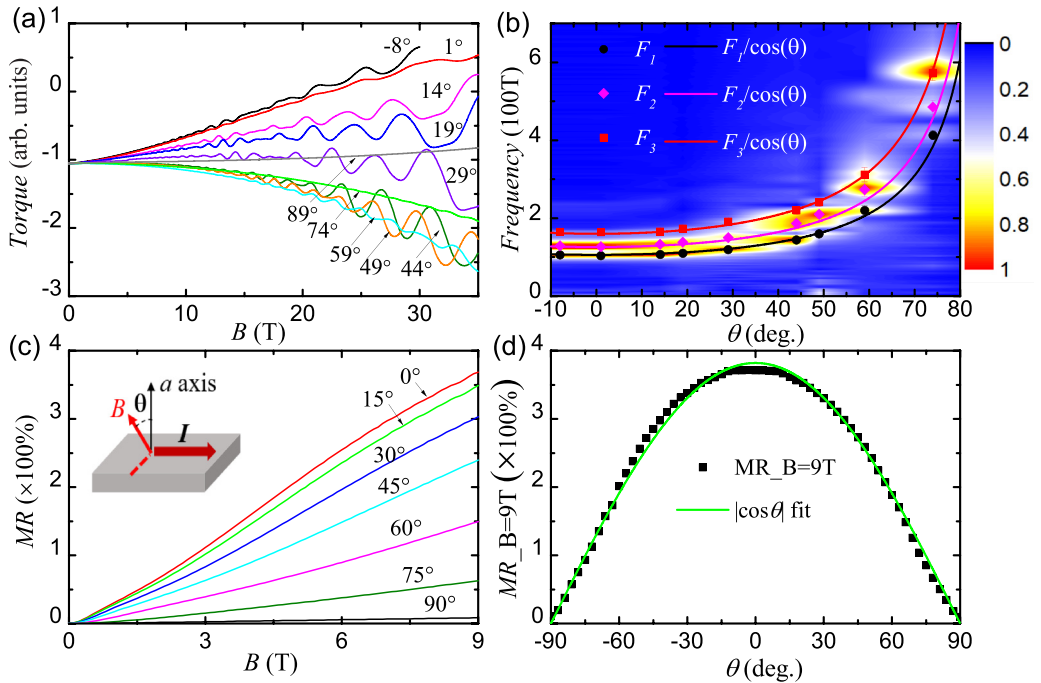
FIG. 3. (a) Field dependence of the magnetic torque measured with different field orientations. (b) The angular dependence of the dHvA oscillation frequency $F(\theta)$ and the fits to $F(\theta) = F_0/|\cos\theta|$. The background is the 2D color plot for angle dependent FFT spectra of the dHvA oscillations. (c) Magnetoresistance of SrZnSb$_2$ measured with different field orientations. Inset: A schematic diagram of the measurement geometry. (d) The angular dependence of resistivity at $B = 9T$ and the $|\cos\theta|$ fit.
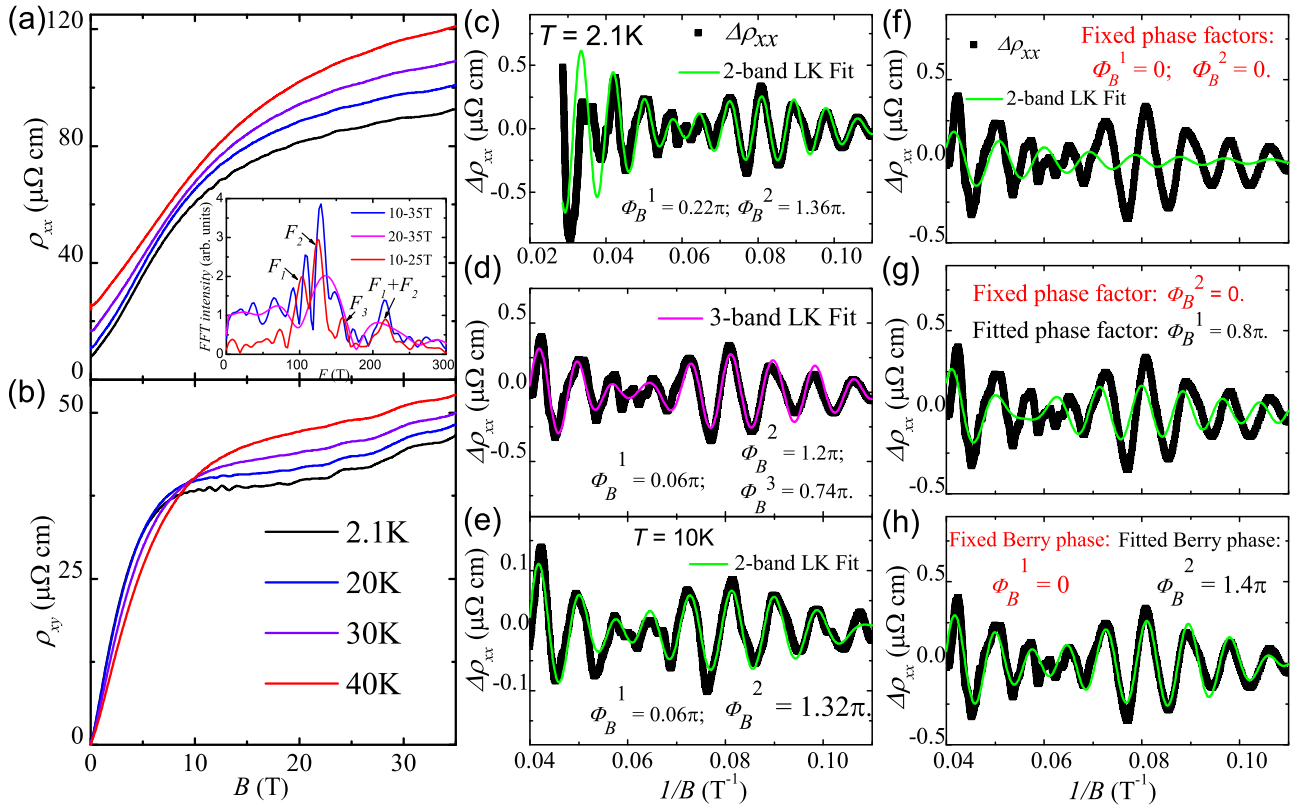
FIG. 4. (a) Field dependence of in-plane resistivity ρ_{xx} of SrZnSb$_2$ measured up to 35 T at different temperatures. Inset: The comparison of the FFT spectra made between 10 T and 35 T, 20 T to 35 T, and 10 T to 25 T at 2 K. (b) Hall resistivity ρ_{xy} up to 35 T measured simultaneously with ρ_{xx}. (c) The oscillatory part of resistivity $\Delta\rho_{xx}$ (black dots) at $T = 2.1$ K and the fit to LK formula with two known frequencies, namely F_1 and F_2. (d) The fit of SdH oscillations at $T = 2.1$ K to LK formula including three frequencies, which are F_1, F_2, and F_3. (e) shows the two-band LK fits of the SdH oscillations at higher temperatures, $T = 10$ K, resulting in similar Berry phases to those of SdH oscillations at $T = 2.1$ K. (f), (g), and (h) are the trials to fit the SdH oscillations at $T = 2.1$ K to two-band LK formula with fixed Berry phase(s) for F_1 and/or F_2. (f) The Berry phases are both fixed to be 0 for F_1 and F_2. (g) Only the Berry phase of F_2 is fixed to be 0, and it's a free fitting parameter for F_1. (h) Only the Berry phase of F_1 is fixed to be 0, and it's a free fitting parameter for F_2.

tilted away and almost vanishes when the field is parallel with the *bc* plane. Figure 3(d) shows the MR measured with the field rotating about the current direction at $B = 9$ T and $T = 2$ K. The result can be well described by $MR \propto |\cos\theta|$, i.e., the MR is only related to the field component perpendicular to the *bc* plane. This has been seen in other 112 material, like Ca/SrMnBi$_2$ [27,60], which confirms the quasi-2D nature of the transport.

To investigate if SrZnSb$_2$ has nontrivial topology, Shubnikov-de Haas (SdH) oscillations have been studied. The in-plane magnetotransport properties with a magnetic field perpendicular to the plane up to 35 T are presented in Fig. 4. ρ_{xx} exhibits linear field dependence at low field ($B < 10$ T) and tends to saturate at high fields with a magnetoresistance (MR) of ~700% at 35 T. ρ_{xy} is positive and linearly dependent with field for $B < 5$ T and then becomes flat at higher fields, indicating multiple band transport nature with the dominant carriers being holes. The change of slope near 10 T implies the variation of densities or mobilities for electron- or holelike carriers at high field range.

As shown in Figs. 4(a) and 4(b), SdH oscillations are observable for both ρ_{xx} and ρ_{xy} when $B > 10$ T. Since Zeeman effect can be observed at high fields, FFT from 10 T to 25 T for the ρ_{xx} at $T = 2.1$ K is made, resulting in the dominant

oscillating frequencies of 103 T and 127 T with a third minor frequency of 160 T [see the inset of Fig. 4(a)], consistent with the values we obtained in dHvA. The SdH oscillations can be described by the LK formula [59]:

$$\Delta\rho \propto B^{\lambda} R_T R_D R_S \cos\left[2\pi\left(\frac{F}{B} + \gamma - \delta\right)\right]$$

where the thermal damping term R_T is equal to $\alpha T\mu/[B\sinh(\alpha T\mu/B)]$ and the Dingle damping factor $R_D = \exp(-\alpha T_D\mu/B)$. μ is the ratio of cyclotron effective mass m^* to the free electron mass m_e and $\alpha = (2\pi^2 k_B m_e)/(\hbar e)$. T_D is the Dingle temperature. $R_S = \cos(\pi g\mu/2)$ is the spin damping factor, where g is the Landau g factor. λ is a dimensional factor, which is $1/2$ for the 3D case and 0 for the 2D case. The phase factor $\gamma - \delta$ of the cosine term is linked with the Berry phase Φ_B by the relation $\gamma = \frac{1}{2} - \frac{\Phi_B}{2\pi}$ [61]. The phase shift δ is 0 for 2D Fermi surfaces and $\pm 1/8$ for 3D ones depending on the FS cross section and the carrier type [62].

To examine the Berry phase accumulated from the cyclotron motions of the quasiparticles in the system, as the FFT spectra are dominated by F_1 and F_2, we first fit the SdH oscillations ($\Delta\rho_{xx}$) at $T = 2.1$ K to the generalized LK formula with two frequencies [63], which we will refer to as
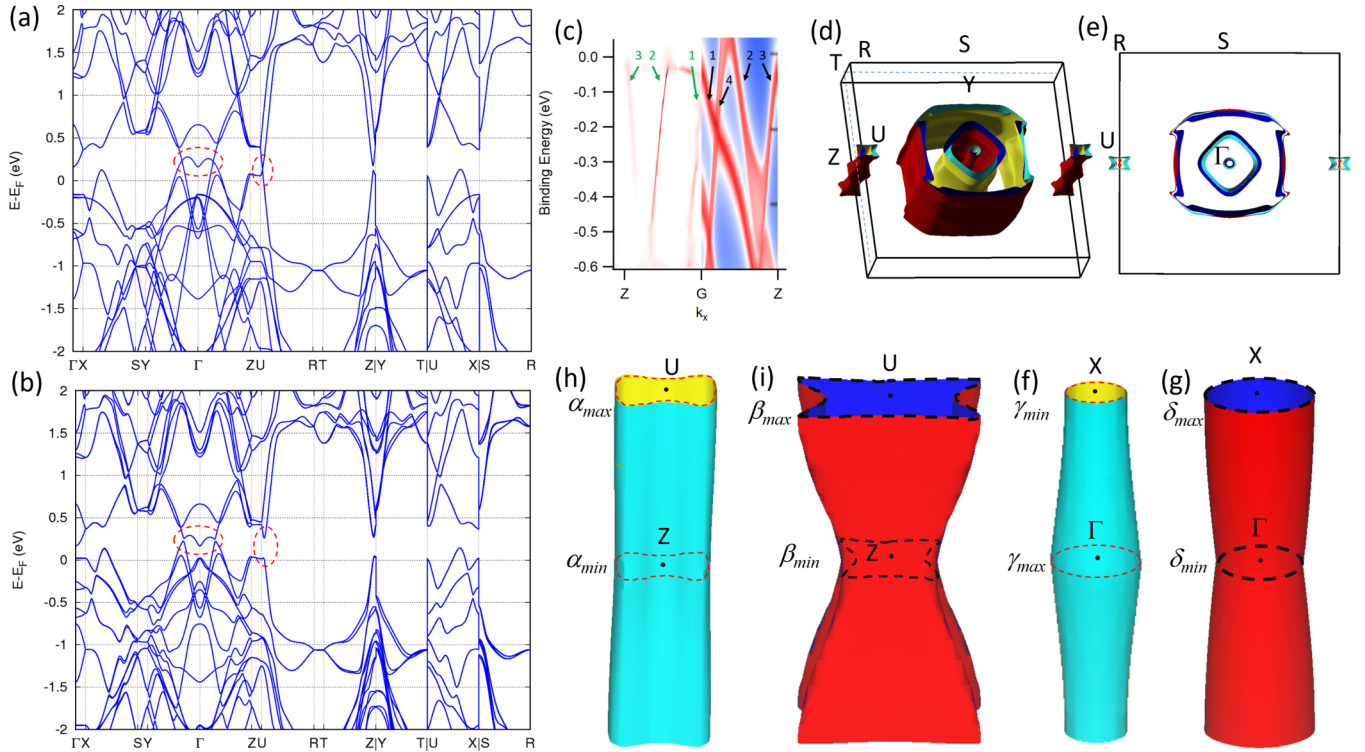
FIG. 5. (a),(b) Band structure of SrZnSb$_2$ without SOC (a) and with SOC (b). The Dirac nodes are circled by red dashed lines. The Fermi level has been adjusted based on the ARPES data. (c) The curvature method processed energy band spectra along Z-Γ-Z line observed in ARPES and the fit with the bands obtained by DFT calculations. (d),(e) Fermi surface of SrZnSb$_2$ from the side (d) and top (e) view. (f)–(i) Individual α, β, γ, and δ Fermi pockets. The maximum and minimum cross section areas of each pocket are circled by the dashed lines.

the two-band LK formula. As seen in Fig. 4(c), the data can be fit well to the two-band LK formula for $1/B > 0.04$ T^{-1}. If the higher field ($B > 25$ T) data is included, the fit cannot converge. This discrepancy between the data and the LK formula fit at high fields probably comes from the Zeeman splitting of the Landau levels. Besides, from the FFT with different field ranges we note that the FFT spectra peaks tend to move to higher values when the higher field range ($B > 25$ T) is included. This gives us a hint that the Zeeman effect appears at high fields. A similar effect has previously been observed in WTe$_2$, where the oscillatory data cannot be reproduced by LK formula for the entire field range because of the strong Zeeman effect at high fields [64]. As such, we focus our fitting at the field range below 25 T where the influence from Zeeman effect should be minimized as evidenced by the high fitting quality. The fitted phase factors $\gamma - \delta$ are 0.39 and 0.82. Considering the 2D Fermi surface revealed from the angular dependence of the oscillations which will be shown later, the δ is taken to be 0. Thus, the obtained Berry phases are 0.22π and 1.36π for F_1 and F_2, respectively. The former indicates a trivial Berry phase for F_1, while the latter represents a nontrivial Berry phase for F_2. We have also tried to include the third minor frequency F_3 for the fitting. The SdH data is fitted by three-band LK formula [Fig. 4(d)]. The obtained Berry phase for F_3 is 0.74π, close to a nontrivial value π. The resulting Berry phases for F_1 and F_2 are $0.06\,\pi$ and $1.2\,\pi$, respectively, which are consistent with those from two-band LK fit in Fig. 4(c). As the three-band LK formula fit does not show notable improvement of the fitting quality, in order to minimize the amount of fitting parameters, we

believe the two-band LK fit should be enough to capture the oscillatory amplitudes and phases of the data.

To check the reliability of the phase factors obtained by the two-band LK fit, we attempted to fit the SdH oscillations at $T = 2.1$ K to the LK formula using fixed phase factors [Fig. 4(f)–4(h)]. In Fig. 4(f), the phase factors $\gamma - \delta$ for both frequencies in two-band LK formula are fixed to 0.5 so that the Berry phases are both trivial. However, as shown clearly the data cannot be fitted at all in this case. In Fig. 4(g), the Berry phase for F_2 is fixed to 0 and the phase factor of F_1 is a free fitting parameter. The best fit gives a significant phase offset between the raw data and the fitting line. Only if the Berry phase for F_1 is fixed to be 0 and the phase factor of F_2 is a free fitting parameter, the data can be well fitted and the obtained Berry phase for F_2 is close to the original two-band LK fit where no phase factor is fixed as seen in Fig. 4(h). Furthermore, to demonstrate the stability of the two-band LK fitting, the same phase factors obtained in Fig. 4(c) are used in the fitting of the SdH oscillations at $T = 10$ K. As shown in Figs. 4(e), these phases factors fit the high temperature data well. A nontrivial Berry phase for F_2 is also extracted by Landau level fan diagram provided in Supplemental Material [65–67]. From the LK fit, we have clearly demonstrated the trivial Berry phase for F_1 and a nontrivial case for F_2 and F_3, suggesting the existence of Dirac fermions.

To better understand the electronic structure of SrZnSb$_2$, we have performed density functional theory (DFT) calculations with and without SOC and discovered that SrZnSb$_2$ is a nodal-line Dirac semimetal. As shown in Fig. 5(a), there

are three Dirac points in the energy band diagram when switching off SOC, which agree well with the results from Refs. [24,68]. The two Dirac points in the Γ-Z line and Γ-Y line are the cross-sectional points of a nodal line lying in the Y-Z plane. This node ring is protected by symmetry operation $\{m_{100}|1/2, 1/2, 1/2\}$ because the two bands, which cross to form this node ring, have opposite eigenvalues of operator $\{m_{100}|1/2, 1/2, 1/2\}$ in the Y-Z plane. In the presence of SOC, this nodal line is gapped because two spin components in the same energy band have opposite eigenvalues of $\{m_{100}|1/2, 1/2, 1/2\}$. The energy gap opened at the nodal line is small, about 30 meV, comparable to 20 meV of the SOC induced gap at the Dirac line nodes in ZrSiS [13]. As shown in Fig. 5(c), the symmetrized Γ-Z ARPES spectra with curvature method [69] (seen in the left half, also seen in Supplementary Figure S2 (a) and (b)) is fit with the bands calculated by DFT [seen in the right half, also seen in Supplemental Fig. S2(c)] [70]. We found that the chemical potential in the DFT calculation results needs to be moved down for 267 meV. The DFT calculation agrees well with the ARPES spectra, showing a strong, dispersive electronlike band crossing at E_F and another electronlike band at the Z point, except that one DFT predicted band [labelled as band 4 in Fig. 5(c)] is not clearly seen in ARPES results, possibly due to a poor matrix element. Based on our calculated band structure and ARPES spectra, the Dirac node is about 200 meV above the Fermi level of our sample.

The Dirac point lying in the U-R line is a double Dirac point formed by the crossing of two doubly degenerate bands without SOC, which is protected by nonsymmorphic symmetry. Following the notion of Ref. [71], the eigenstates of the two crossing bands belong to the representation of $P_1 + P_3$ and $P_2 + P_4$, respectively, leading to crossing of the two bands rather than anticrossing. When SOC is included, we find the bands along U-R remain fourfold degenerate considering spin component. However, there is only one irreducible representation along the U-R line in this situation. As such, the crossing of each pair of bands is forbidden and the Dirac point in this line is gapped accordingly. The energy gap is about 230 meV. In addition, we note that this Dirac point is quasi-2D since both its conduction and valence bands have nearly flat dispersions along the Z-U direction.

As mentioned before, we determine the Fermi level for the sample by adjusting the DFT energy bands with those from ARPES alongthe Z-Γ-Z line, as shown in Fig. 5(c). We obtain an experimental Fermi energy E_F to be 267 meV lower than the theoretical value, consistent with the observation that the transport properties are dominated by holes. This shifted E_F may be caused by possible Sr/Zn deficiencies in the sample. Based on the adjusted E_F, we plot the Fermi surface in Figs. 5(d) and 5(e). One should keep in mind that this Fermi energy cuts two valence bands, resulting in two sets of Fermi surface of similar shape with one set nested into the other.

All Fermi surfaces are 2D like with slight corrugation along the k_x direction, consistent with the 2D nature of the fermiology revealed by our dHvA data. The three oscillation frequencies observed in our quantum oscillations can only come from the two small nontrivial Fermi pockets α and β centering at the BZ edge Y point and the other two small trivial Fermi pockets centering at the BZ center Γ point, as

TABLE III. The comparison of oscillation frequencies obtained from DFT calculations and experimental observations with $B//a$ axis of SrZnSb$_2$. To avoid the effect of Zeeman effect on the data analysis, FFT was done on the SdH data (5 T to 15 T) and dHvA data (10 T to 25 T). Based on the DFT calculations, α and β Fermi pockets have nontrivial topology while γ and δ Fermi pockets are trivial.

	$\alpha_{\min}$	$\alpha_{\max}$	$\beta_{\min}$	$\beta_{\max}$	$\gamma_{\min}$	$\gamma_{\max}$	$\delta_{\min}$	$\delta_{\max}$
F^{DFT} (T)	109	125	153	368	47	106	115	183
F^{dHvA} (T)		127	160			103		
F^{SdH} (T)		127	160			103		
m^{dHvA} (m_e)		0.1	0.09			0.1		
Φ^{SdH}		1.2π	0.74π			0.06π		

shown in Figs. 5(f)–5(i). We have calculated the frequencies associated with the extreme area of these four Fermi pockets using the code provided by Ref. [72] and summarized them in Table III.

IV. DISCUSSION

Here we would like to have more discussions on the Berry phase for the three frequencies observed from QO. In theory, F_1 from a trivial Fermi surface should correspond to a Berry phase (ϕ_B) of 0, which is consistent with our experimental value $\phi_B^\alpha = 0.06\pi$. Each of the Fermi surfaces that are responsible for F_2 and F_3 includes two equivalent Dirac points. As is mentioned above, these Dirac points are quasi-2D, so every Dirac point should contribute a Berry phase of π similar to the case of graphene. Two Dirac points will lead to a Berry phase of 2π for both F_2 and F_3. However, the gaps opened at the two Dirac points will alter the Berry phase according to the equation $\phi_B = \pm 2\pi(1 - \Delta/2E_{FC})$, where Δ is the gap size and E_{FC} represents energy difference between Fermi energy and the center of energy gap [62]. The Berry phases for F_2 and F_3 are estimated to be 1.57π and 0.36π, respectively. It's worth noting that a 0.3π deviation of Berry phase from π was previously observed due to nonideal linear dispersion in NbP [67]. This explains why the Berry phases we obtained from quantum oscillations are not close to π for F_2 and F_3, while it clearly shows that the Fermi surfaces that are responsible for the two frequencies are topological nontrivial.

Since the nodal-line and nodal features are about 200 meV above the FL in our SrZnSb$_2$ sample, our current ARPES experiments only observe linear dispersive bands but not the nodal features, however, our comprehensive study of QO, DFT, and ARPES data can unambiguously prove the existence of the nontrivial topology. In future study, the sample will be electron doped by substituting La into the Sr sites to tune the FL above the nodal features and then ARPES will be performed to investigate the emergent phenomena associated with the topological nodal line, such as the drumhead states, etc.

Finally, to understand the role of magnetism in the $AMnX_2$ materials, we compare the relativistic fermion transport properties between SrZnSb$_2$ and its magnetic version Sr$_{1-y}$Mn$_{1-z}$Sb$_2$ [33]. The two compounds have the same orthorhombic crystal structure with a space group of *Pnma*, and the Sb square nets are distorted in both compounds.

In $Sr_{1-y}Mn_{1-z}Sb_2$, the canted AFM order of Mn moments coexists with the topological state hosted by Sb distorted square net layers. As a result, the relativistic transport properties, including the amplitude and frequency of the SdH oscillations, are coupled with the FM component. In both materials, the Fermi surfaces that consist of relativistic fermions are quasi-2D like. However, because of the lack of AFM layers between two neighboring distorted Sb square net layers, the resistivity anisotropy of $SrZnSb_2$ is much weaker. Further doping studies of $SrMn_{1-x}Zn_xSb_2$ would be beneficial for understanding the effect of magnetism on Dirac fermion transport in the system.

V. CONCLUSIONS

In conclusion, we have performed a comprehensive study of the quantum transport properties and the electronic structure of $SrZnSb_2$ with a combination of the magnetotransport measurements, first-principles calculations, and ARPES experiment. From the analysis of quantum oscillations, low effective masses and nontrivial Berry phases are revealed. These quantum oscillations are revealed to be associated with the small trivial Fermi pockets in the BZ center and the nontrivial Fermi pockets in the BZ edge. In addition, a node line surrounding the BZ center with a tiny SOC gap is suggested by the first-principles calculations.

[1] X. L. Qi and S. C. Zhang, Rev. Mod. Phys. **83**, 1057 (2011).

[2] Z. Wang, Y. Sun, X. Q. Chen, C. Franchini, G. Xu, H. Weng, X. Dai, and Z. Fang, Phys. Rev. B **85**, 195320 (2012).

[3] Z. Wang, H. Weng, Q. Wu, X. Dai, and Z. Fang, Phys. Rev. B **88**, 125427 (2013).

[4] Z. K. Liu, B. Zhou, Y. Zhang, Z. J. Wang, H. M. Weng, D. Prabhakaran, S.-K. Mo, Z. X. Shen, Z. Fang, X. Dai, Z. Hussain, and Y. L. Chen, Science **343**, 864 (2014).

[5] Z. K. Liu, J. Jiang, B. Zhou, Z. J. Wang, Y. Zhang, H. M. Weng, D. Prabhakaran, S. Mo, H. Peng, P. Dudin, T. Kim, M. Hoesch, Z. Fang, X. Dai, Z. X. Shen, D. L. Feng, Z. Hussain, and Y. L. Chen, Nat. Mater. **13**, 677 (2014).

[6] M. Neupane, S.-Y. Xu, R. Sankar, N. Alidoust, G. Bian, C. Liu, I. Belopolski, T.-R. Chang, H.-T. Jeng, H. Lin, A. Bansil, F. Chou, and M. Z. Hasan, Nat. Commun. **5**, 3786 (2014).

[7] S. Borisenko, Q. Gibson, D. Evtushinsky, V. Zabolotnyy, B. Buchner, and R. J. Cava, Phys. Rev. Lett. **113**, 027603 (2014).

[8] T. Liang, Q. Gibson, M. N. Ali, M. Liu, R. J. Cava, and N. P. Ong, Nat. Mater. **14**, 280 (2015).

[9] H. Weng, C. Fang, Z. Fang, B. A. Bernevig, and X. Dai, Phys. Rev. X **5**, 011029 (2015).

[10] B. Q. Lv, H. M. Weng, B. B. Fu, X. P. Wang, H. Miao, J. Ma, P. Richard, X. C. Huang, L. X. Zhao, G. F. Chen, Z. Fang, X. Dai, T. Qian, and H. Ding, Phys. Rev. X **5**, 031013 (2015).

[11] S. Y. Xu, I. Belopolski, N. Alidoust, M. Neupane, G. Bian, C. Zhang, R. Sankar, G. Chang, Z. Yuan, C. C. Lee, S. M. Huang, H. Zheng, J. Ma, D. S. Sanchez, B. K. Wang, A. Bansil, F. Chou, P. P. Shibayev, H. Lin, S. Jia, and M. Z. Hasan, Science **349**, 613 (2015).

[12] Q. Xu, Z. Song, S. Nie, H. Weng, Z. Fang, and X. Dai, Phys. Rev. B **92**, 205310 (2015).

[13] L. M. Schoop, M. N. Ali, C. Straßer, A. Topp, A. Varykhalov, D. Marchenko, V. Duppel, S. S. P. Parkin, B. V. Lotsch, and C. R. Ast, Nat. Commun. **7**, 11696 (2016).

[14] G. Bian, T.-R. Chang, R. Sankar, S.-Y. Xu, H. Zheng, T. Neupert, C.-K. Chiu, S.-M. Huang, G. Chang, I. Belopolski, D. S. Sanchez, M. Neupane, N. Alidoust, C. Liu, B. Wang, C.-C. Lee, H.-T. Jeng, C. Zhang, Z. Yuan, S. Jia, A. Bansil, F. Chou, H. Lin, and M. Z. Hasan, Nat. Commun. **7**, 10556 (2016).

[15] Y. Wu, L. L. Wang, E. Mun, D. D. Johnson, D. Mou, L. Huang, Y. Lee, S. L. Bud'ko, P. C. Canfield, and A. Kaminski, Nat. Phys. **12**, 667 (2016).

[16] J. Hu, Z. Tang, J. Liu, X. Liu, Y. Zhu, D. Graf, K. Myhro, S. Tran, C. N. Lau, J. Wei, and Z. Mao, Phys. Rev. Lett. **117**, 016602 (2016).

[17] A. Yamakage, Y. Yamakawa, Y. Tanaka, and Y. Okamoto, J. Phys. Soc. Jpn. **85**, 013708 (2016).

[18] E. Emmanouilidou, B. Shen, X. Deng, T.-R. Chang, A. Shi, G. Kotliar, S.-Y. Xu, and N. Ni, Phys. Rev. B **95**, 245113 (2017).

[19] A. A. Soluyanov, D. Gresch, Z. Wang, Q. Wu, M. Troyer, X. Dai, and B. A. Bernevig, Nature (London) **527**, 495 (2015).

[20] L. Huang, T. M. McCormick, M. Ochi, Z. Zhao, M. T. Suzuki, R. Arita, Y. Wu, D. Mou, H. Cao, J. Yan, N. Trivedi, and A. Kaminski, Nat. Mater. **15**, 1155 (2016).

[21] Y. Wu, D. Mou, N. H. Jo, K. Sun, L. Huang, S. L. Bud'ko, P. C. Canfield, and A. Kaminski, Phys. Rev. B **94**, 121113(R) (2016).

[22] C. Wang, Y. Zhang, J. Huang, S. Nie, G. Liu, A. Liang, Y. Zhang, B. Shen, J. Liu, C. Hu, Y. Ding, D. Liu, Y. Hu, S. He, L. Zhao, L. Yu, J. Hu, J. Wei, Z. Mao, Y. Shi, X. Jia, F. Zhang, S. Zhang, F. Yang, Z. Wang, Q. Peng, H. Weng, X. Dai, Z. Fang, Z. Xu, C. Chen, and X. J. Zhou, Phys. Rev. B **94**, 241119(R) (2016).

[23] N. P. Armitage, E. J. Mele, and A. Vishwanath, Rev. Mod. Phys. **90**, 015001 (2018).

[24] B. Bradlyn, L. Elcoro, J. Cano, M. G. Vergniory, Z. Wang, C. Felser, M. I. Aroyo, and B. A. Bernevig, Nature (London) **547**, 298 (2017).

[25] L. M. Schoop, F. Pielnhofer, and B. V. Lotsch, Chem. Mater. **30**, 3155 (2018).

[26] J. Park, G. Lee, F. Wolff-Fabris, Y. Y. Koh, M. J. Eom, Y. K. Kim, M. A. Farhan, Y. J. Jo, C. Kim, J. H. Shim, and J. S. Kim, Phys. Rev. Lett. **107**, 126402 (2011).

[27] K. Wang, D. Graf, L. Wang, H. Lei, S. W. Tozer, and C. Petrovic, Phys. Rev. B **85**, 041101(R) (2012).

[28] S. Borisenko, D. Evtushinsky, Q. Gibson, A. Yaresko, K. Koepernik, T. Kim, M. Ali, J. van den Brink, M. Hoesch, A. Fedorov, E. Haubold, Y. Kushnirenko, I. Soldatov, R. Schäfer, and R. J. Cava, Nat. Commun. **10**, 3424 (2019).

[29] H. Masuda, H. Sakai, M. Tokunaga, Y. Yamasaki, A. Miyake, J. Shiogai, S. Nakamura, S. Awaji, A. Tsukazaki, H. Nakao, Y. Murakami, T. Arima, Y. Tokura, and S. Ishiwata, Sci. Adv. **2**, e1501117 (2016).

[30] L. Li, K. Wang, D. Graf, L. Wang, A. Wang, and C. Petrovic, Phys. Rev. B **93**, 115141 (2016).

[31] Y.-Y. Wang, Q.-H. Yu, and T.-L. Xia, Chinese Phys. B **25**, 107503 (2016).

[32] J. Liu, J. Hu, H. Cao, Y. Zhu, A. Chuang, D. Graf, D. J. Adams, S. M. A. Radmanesh, L. Spinu, I. Chiorescu, and Z. Mao, Sci. Rep. **6**, 30525 (2016).

[33] J. Y. Liu, J. Hu, Q. Zhang, D. Graf, H. B. Cao, S. M. A. Radmanesh, D. J. Adams, Y. L. Zhu, G. F. Cheng, X. Liu, W. A. Phelan, J. Wei, M. Jaime, F. Balakirev, D. A. Tennant, J. F. DiTusa, I. Chiorescu, L. Spinu, and Z. Q. Mao, Nat. Mater. **16**, 905 (2017).

[34] J. B. He, Y. Fu, L. X. Zhao, H. Liang, D. Chen, Y. M. Leng, X. M. Wang, J. Li, S. Zhang, M. Q. Xue, C. H. Li, P. Zhang, Z. A. Ren, and G. F. Chen, Phys. Rev. B **95**, 045128 (2017).

[35] S. Huang, J. Kim, W. A. Shelton, E. W. Plummer, and R. Jin, Proc. Natl. Acad. Sci. **114**, 6256 (2017).

[36] Y. Y. Wang, S. Xu, L. L. Sun, and T. L. Xia, Phys. Rev. Mater. **2**, 021201 (2018).

[37] R. Kealhofer, S. Jang, S. M. Griffin, C. John, K. A. Benavides, S. Doyle, T. Helm, P. J. W. Moll, J. B. Neaton, J. Y. Chan, J. D. Denlinger, and J. G. Analytis, Phys. Rev. B **97**, 045109 (2018).

[38] J. Hu, Y. L. Zhu, D. Graf, Z. J. Tang, J. Y. Liu, and Z. Q. Mao, Phys. Rev. B **95**, 205134 (2017).

[39] L. M. Schoop, A. Topp, J. Lippmann, F. Orlandi, L. Müchler, M. G. Vergniory, Y. Sun, A. W. Rost, V. Duppel, M. Krivenkov, S. Sheoran, P. Manuel, A. Varykhalov, B. Yan, R. K. Kremer, C. R. Ast, and B. V. Lotsch, Sci. Adv. **4**, eaar2317 (2018).

[40] Y. F. Guo, A. J. Princep, X. Zhang, P. Manuel, D. Khalyavin, I. I. Mazin, Y. G. Shi, and A. T. Boothroyd, Phys. Rev. B **90**, 075120 (2014).

[41] M. Chinotti, A. Pal, W. J. Ren, C. Petrovic, and L. Degiorgi, Phys. Rev. B **94**, 245101 (2016).

[42] J. Y. Liu, J. Hu, D. Graf, T. Zou, M. Zhu, Y. Shi, S. Che, S. M. A. Radmanesh, C. N. Lau, L. Spinu, H. B. Cao, X. Ke, and Z. Q. Mao, Nat. Commun. **8**, 646 (2017).

[43] A. Zhang, C. Liu, C. Yi, G. Zhao, T. Xia, J. Ji, Y. Shi, R. Yu, X. Wang, C. Chen, and Q. Zhang, Nat. Commun. **7**, 13833 (2016).

[44] Y. Wang, P. Guo, Q. Yu, S. Xu, K. Liu, and T. Xia, New J. Phys. **19**, 123044 (2017).

[45] W. Ren, A. Wang, D. Graf, Y. Liu, Z. Zhang, W. G. Yin, and C. Petrovic, Phys. Rev. B **97**, 035147 (2018).

[46] K. Zhao, E. Golias, Q. H. Zhang, M. Krivenkov, A. Jesche, L. Gu, O. Rader, I. I. Mazin, and P. Gegenwart, Phys. Rev. B **97**, 115166 (2018).

[47] K. Wang and C. Petrovic, Appl. Phys. Lett. **101**, 152102 (2012).

[48] E. Brechtel, G. Cordier, and H. Schäfer, Z. Naturforsch. **34**, 251 (1979).

[49] K. D. Myers, S. L. Budko, I. R. Fisher, Z. Islam, H. Kleinke, A. H. Lacerda, and P. C. Canfield, J. Magn. Magn. Mater. **205**, 27 (1999).

[50] C. Song, Jaehyun Park, Japil Koo, K.-B. Lee, J. Y. Rhee, S. L. Budko, P. C. Canfield, B. N. Harmon, and A. I. Goldman, Phys. Rev. B **68**, 035113 (2003).

[51] Rigaku, CrystalClear, Rigaku Corporation, Tokyo, Japan, 2005.

[52] G. M. Sheldrick, Acta Crystallogr. A **64**, 112 (2008).

[53] K. Momma and F. Izumi, J. Appl. Crystallogr. **41**, 653 (2008).

[54] J. Rodriguez-Carvajal, Physica B **192**, 55 (1993).

[55] G. Kresse and D. Joubert, Phys. Rev. B **59**, 1758 (1999).

[56] J. P. Perdew, K. Burke, and M. Ernzerhof, Phys. Rev. Lett. **77**, 3865 (1996).

[57] G. Kresse and J. Furthmüller, Comput. Mater. Sci. **6**, 15 (1996).

[58] A. Wang, D. Graf, L. Wu, K. Wang, E. Bozin, Y. Zhu, and C. Petrovic, Phys. Rev. B **94**, 125118 (2016).

[59] D. Shoenberg, *Magnetic Oscillations in Metals* (Cambridge Univ. Press, Cambridge, 1984).

[60] K. Wang, D. Graf, H. Lei, S. W. Tozer, and C. Petrovic, Phys. Rev. B **84**, 220401(R) (2011).

[61] G. P. Mikitik and Y. V. Sharlai, Phys. Rev. Lett. **82**, 2147 (1999).

[62] C. Li, C. M. Wang, B. Wan, X. Wan, H. Z. Lu, and X. C. Xie, Phys. Rev. Lett. **120**, 146602 (2018).

[63] J. Hu, J. Y. Liu, D. Graf, S. M. A. Radmanesh, D. J. Adams, A. Chuang, Y. Wang, I. Chiorescu, J. Wei, L. Spinu, and Z. Q. Mao, Sci. Rep. **6**, 18674 (2016).

[64] D. Rhodes, S. Das, Q. R. Zhang, B. Zeng, N. R. Pradhan, N. Kikugawa, E. Manousakis, and L. Balicas, Phys. Rev. B **92**, 125152 (2015).

[65] See Supplemental Material at http://link.aps.org/supplemental/10.1103/PhysRevB.100.195123 for the Berry phase extraction by Landau level fan diagram.

[66] J. Xiong, Y. Luo, Y. H. Khoo, S. Jia, R. J. Cava, and N. P. Ong, Phys. Rev. B **86**, 045314 (2012).

[67] Z. Wang, Y. Zheng, Z. Shen, Y. Lu, H. Fang, F. Sheng, Y. Zhou, X. Yang, Y. Li, C. Feng, and Z. A. Xu, Phys. Rev. B **93**, 121112(R) (2016).

[68] T. Zhang, Y. Jiang, Z. Song, H. Huang, Y. He, Z. Fang, H. Weng, and C. Fang, Nature (London) **566**, 475 (2019).

[69] P. Zhang, P. Richard, T. Qian, Y.-M. Xu, X. Dai, and H. Ding, Rev. Sci. Instrum. **82**, 043712 (2011).

[70] See Supplemental Material at http://link.aps.org/supplemental/10.1103/PhysRevB.100.195123 for the detailed band structure along Z-Γ-Z obtained from ARPES and first-principles calculations.

[71] M. I. Aroyo, A. Kirov, C. Capillas, J. M. Perez-Mato, and H. Wondratschek, Acta Crystallogr. Sect. A **62**, 115 (2006).

[72] S. R. Julian, Comput. Phys. Commun. **183**, 324 (2012).